energies

MDPI

Article

Experimental Study of Impingement Effusion-Cooled Double-Wall Combustor Liners: Thermal Analysis

Thomas Jackowski †,‡, Maximilian Elfner *,‡ and Hans-Jörg Bauer ‡

Institute of Thermal Turbomachinery (ITS), Karlsruhe Institute of Technology (KIT), 76137 Karlsruhe, Germany; thomas.jackowski@kit.edu (T.J.); hans-joerg.bauer@kit.edu (H.-J.B.)

* Correspondence: maximilian.elfner@kit.edu; Tel.: +49-721-608-43634

† He had Retired from KIT.

‡ These authors contributed equally to this work.

Abstract: A new experimental study is presented for a combustor with a double-wall cooling design. The inner wall at the hot gas side features effusion cooling with 7-7-7 laidback fan-shaped holes, and the outer wall at the cold side features an impingement hole pattern with circular holes. Data have been acquired to assess the thermal and aerodynamic behavior of the setup using a new, scaled up, engine-similar test rig. Similarity includes Reynolds, Nusselt, and Biot numbers for hot gas and coolant flow. Different geometrical setups are studied by varying the cavity height between the two walls and the relative alignment of the two hole patterns at several different blowing ratios. This article focuses on the thermal performance of the setup. The temperature data are acquired using two infrared systems on either side of the effusion wall specimen. In addition to cooling effectiveness evaluations, finite element simulations are performed, yielding the locally resolved wall heat fluxes. Results are presented for three cavity heights and two longitudinal specimen alignments. The results show that the hot gas side total cooling effectiveness can achieve values as high as 90% and is mainly influenced by the effusion coverage. Impingement cooling has a small influence on overall effectiveness, and the area of influence is mainly located upstream where effusion cooling is not built up completely. The analyzed geometric variations show a major influence on cavity flow and impingement heat transfer. Small cavities lead to constrained flow and high local Nusselt numbers, while larger cavities show more equalized Nusselt number distributions. A present misalignment shows especially high influence at small cavity heights. The largest cavity height, in general, showed a decrease in heat transfer due to reduced jet momentum.

Keywords: combustor cooling; effusion impingement; thermography

Citation: Jackowski, T.; Elfner, M.; Bauer, H.-J. Experimental Study of Impingement Effusion-Cooled Double-Wall Combustor Liners: Thermal Analysis. *Energies* **2021**, *14*, 4843. https://doi.org/10.3390/en14164843

Academic Editors: Antonio Andreini, Lorenzo Mazzei, Chanwoo Park and Andrea De Pascale

Received: 7 June 2021
Accepted: 31 July 2021
Published: 9 August 2021

1. Introduction

The continuous development of aero-gas turbines leads to constant improvements that benefit air passengers and the environment. The development of new combustor technologies and the improvement of existing concepts are key to reaching new target efficiencies. A commonly used combustion technology to reduce the formation of nitrogen oxides (NO_x) is the Rich-Quench-Lean (RQL) combustor describing the three major combustion regions in an annular combustor.

As shown in Figure 1, the air from the compressor is divided into two major flow paths. A small amount of the compressor air is used to create an air-assisted fuel spray, providing a minimal amount air for burning that fuel spray in a rich environment (red arrow). The remaining air is guided around the combustor liner and used for consecutive mixing and dilution and mainly for the cooling of the liner walls.

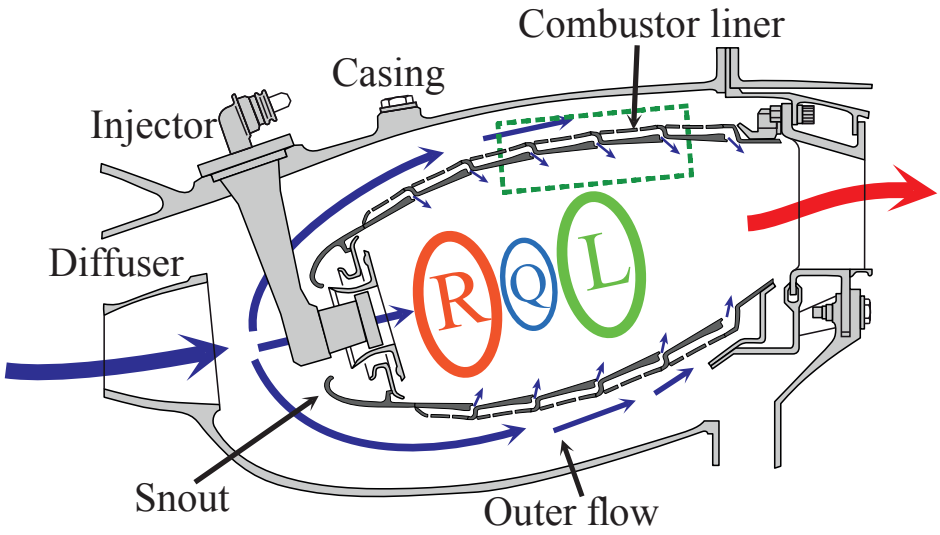

Figure 1. Double-Wall design study adapted from V2500 combustor. The compressed air (blue) is divided between combustor liner and outer flow. The air in the outer flow acts as mixing air and coolant, while the combustor liner air is used for primary combustion (red). Green area marks the region of interest for this study.

Many different cooling schemes exist to allow for the protection of the combustor walls which are exposed to flame temperatures varying from 1700 to 2500 K. The cooling schemes have to be adapted to the combustor design and thermal load. A good overview is given in [1] (p. 3). New lean combustion technologies (e.g., Lazik et al. [2] present the development of lean-burn combustion technology with an internally staged lean direct injection (LDI) injector) require an increased amount of air for the injector and mixing process, which results in less available air for wall cooling. Standard film cooling integrated in the wall of the combustor liner shows too low of a cooling effectiveness at those low blowing ratios. With a pressure drop of $\Delta p/p \approx 3$–4% between outer flow and inner flow, impingement effusion cooling can protect the metal parts more effectively with higher cooling efficiencies. The concept implements a double-wall for the combustor liner, where an initial stage of impingement cooling is followed by an effusion cooling scheme for the innermost wall. In addition to an increase in total cooling effectiveness, a new degree of freedom for design is introduced which allows the distribution of the pressure drop over the two walls, allowing for the optimization of effusion cooling.

This article presents an extensive experimental investigation of the thermal behavior of such a cooling design. An engine-similar test rig is presented which allows for the determination of wall temperatures on both sides of the liner wall and subsequently the computation of heat fluxes. The presented results show the effects of varying operating conditions and different geometrical setups, mainly the cavity height between the double-walls and the relative positioning of impingement and effusion holes.

An additional article with an extensive flow analysis using high-speed stereo particle image velocimetry will be prepared for publication, the tentative title of which is "Experimental Study of Impingement Effusion Cooled double-wall Combustor Liners: Aerodynamic Analysis with Stereo-PIV".

1.1. Impingement Effusion Cooling Methods for Combustor Walls

Combining impingement and effusion cooling in a double-wall arrangement can meet the technical requirements in lean burn combustors and thus is one of the preferred cooling schemes. Sweeney and Rhodes [3] experimentally investigate a turbine airfoil cooled by using a scaled wall element in a *Lamilloy*® (Rolls Royce Allison) design. The single wall element has internal flow channels virtually creating an impingement cooling scheme and an effusion cooling scheme in a flat double-wall setup.

Andrews et al. [4] carry out experiments to investigate the overall wall heat transfer for an impingement and effusion cooled wall. The authors conclude with an increased heat transfer with both cooling methods combined compared to applying impingement cooling alone.

The effects of geometrical arrangement between impingement and effusion cooling holes was studied by Al Dabagh et al. [5]. Additionally, a variation of hole size by maintaining the amount of holes was performed. They show that an equal amount of impingement and effusion cooling should be favored as it provides the best ratio of heat transfer coefficient to coolant usage. Nazari et al. [6] investigated the same topic by performing conjugate heat transfer calculations with computational fluid dynamic (CFD) methods. A similar calculation has been presented by Oguntade et al. [7] with reduced mass flows. All authors agree that impingement cooling can increase total cooling effectiveness, especially in the early upstream effusion region where the exterior coolant film is not yet deployed. The main cooling contribution, especially downstream, is introduced by the effusion cooling on the hot gas side.

Different impingement and effusion double-wall configurations were experimentally investigated by Martiny et al. [8] under scaled conditions and realistic density ratios. Two specimens were introduced and compared by the overall cooling effectiveness and the separate contribution of either the impingement or effusion cooling effect. The results show that especially in the upstream region at the beginning of the cooling film build up, the impingement cooling provides a gain in overall cooling effectiveness of around 15%. This can be observed for both specimen configurations.

A full coverage effusion cooling using slot cooling ejection of a combustor liner was investigated by Andreini et al. [9] for various density ratios *DR* between coolant and hot gas under scaled conditions. While maintaining the same blowing ratio *M* and increasing the density ratio, the heat transfer was lower. The authors proposed that keeping the velocity ratio *VR* is more favorable to creating comparable results. Cocchi et al. [10] investigated two geometries of a double-wall cooling scheme experimentally and using CFD. Hole pattern geometries were comparable with the ones used in this study. They show an influence of longitudinal pattern shift mainly on the heat transfer coefficient on the inner effusion wall. Chen et al. [11] carried out CFD calculations only for a similar cooling setup but introduced cross flow for the coolant between the inner and outer wall. The results are comparable.

In [12–17], a series of experiments were carried out to investigate the full-coverage effusion cooling of a combustor wall with internal impingement cooling. Tests were either performed with effusion cooling only and internal cross flow or using a second internal wall with impingement holes and a plenum feed and optional cross flow. Additionally, main flow acceleration can be introduced. The results are compared by using the adiabatic cooling effectiveness, heat transfer coefficients, and aerodynamic data for blowing ratios of $M = 3.3$–7.4 at a density ratio of DR ≈ 1.05. Results are in agreement with previous studies, with the main new feature being the simultaneously acquired data on either side of the effusion specimen. Cross flow leads, in general, to a deterioration of hot side cooling effectiveness.

Apart from combustor wall cooling research, the application of effusion and impingement cooling is also considered for turbine airfoils. Ngetich et al. [18,19] investigate the possible application of said cooling method to turbine airfoils and conduct experiments to asses the adiabatic cooling effectiveness with pressure sensitive paint. In a similar setup, Murray et al. [20–22] conducted numerical and experimental investigations for walls with combined impingement and effusion cooling methods and developed methods to evaluate cooling performance of cooling schemes with double-walls.

Shrager et al. [23,24] perform thermal and aerodynamic analysis of a double-wall combustor liner. While the general impingement effusion setup is comparable, they focus on the area of dilution holes which are not included in this article's setup. Beside extensive analysis of the area close to the dilution holes, they show high total cooling effectivenesses on the hot gas surface, mainly influence by effusion cooling. Huelsmann et al. [25] analyze

the relative location of an impingement jet to an effusion hole inflow in a similar setup. While varying jet to effusion distance and angular position, they focus on the convective heat transfer in the effusion hole. They show an increase in convective heat transfer by up to 20–30% compared to a fully developed pipe flow.

The test setup used for this article has been analyzed using a conjugated heat transfer numerical approach [26]. The results indicate that the strongest effect on cooling effectiveness is introduced by the blowing ratio. After a short distance downstream of the initial effusion holes, the effusion cooling is of higher importance than the internal impingement cooling. On the internal side, a strong fluctuation of Nusselt numbers can be observed due to impinging jets. Both these findings agree well with the previously shown studies and also with the results presented in this article.

2. Experimental Methodology

Aerothermal testing of gas turbine components is usually performed under scaled laboratory conditions. The rig pressures are close to ambient pressure and applied temperatures are considerably lower. A geometric upscaling is performed to allow better access and resolution of applied measurement techniques.

With respect to conjugate heat transfer, it is important to achieve thermal similarity in order to obtain comparable results that can be applied to real gas turbine components. For film cooling applications (e.g., the effusion side of the specimen), the wall temperature is evaluated in relation to the far field hot gas temperature T_∞ and the internal coolant temperature $T_{c,int}$, defining the total cooling effectiveness:

$$\phi = \frac{T_\infty - T_w}{T_\infty - T_{c,int}}. \tag{1}$$

The heat transfer coefficient is of particular interest in film cooling design. The superposition approach to film cooling [27,28] determines the adiabatic wall temperature T_{aw} as the driving temperature of the heat flux q'' with the heat transfer coefficient with film cooling h_f:

$$q'' = h_f(T_{aw} - T_w). \tag{2}$$

In stationary application, the convective heat flux from the cooling film into the wall equals the heat flux through the wall. As proposed in [29], setting the convective heat flux from Equation (2) equal to the conductive wall heat flux with 1-D assumption results in

$$q'' = h_f(T_{aw} - T_w) = \frac{T_{aw} - T_{c,int}}{\frac{1}{h_f} + \frac{t}{k} + \frac{1}{h_{c,int}}} \Leftrightarrow \frac{T_{aw} - T_w}{T_{aw} - T_{c,int}} = \frac{1}{1 + \mathrm{Bi} + \frac{h_f}{h_{c,int}}} \tag{3}$$

through a wall with the thickness t and heat conductivity k. For a correct thermal scaling, Equation (3) shows the necessity of respecting the hot gas Biot number and the ratio of $h_f/h_{c,int}$. Coolant warming can be accounted for if needed [30]. Depending on the operating parameters in the experiment, it can be reasonable and necessary to substitute the specimen materials to achieve Biot number similarity. For a cooled turbine blade, Albert et al. [29] identified the Biot number to be $\mathrm{Bi} \approx 0.4$. The setup used for this article achieves this similarity and is described in the following.

2.1. Experimental Setup

The test rig consists of two rectangular channel sections that are connected together through a cavity in which a combustor double-wall is simulated. Measurements focus on impingement cooling in combination with effusion cooling and are performed under scaled aerothermal and aerodynamic conditions. Infrared measurement techniques will be used to derive cooling and heat flux quantities.

The infrastructure to drive the test section is shown in Figure 2, left side. For the open loop main flow, the air is provided by a radial compressor, which is capable of

providing a mass flow of 3 kg/s at a pressure ratio of 1.4. The air can be heated by electrical heaters with a maximum power of 450 kW. The power for each individual heater element (16 kW) is controlled through a Programmable-Logic-Controller-based proportional–integral–derivative (PID) controller by measuring the exit temperature of the air at each element, yielding a well mixed and uniform exit temperature. After heating, the air passes additional mixers, screens, and meshes to further improve temperature and velocity uniformity. Eventually the airflow is accelerated through a nozzle to achieve the target hot gas Reynolds number.

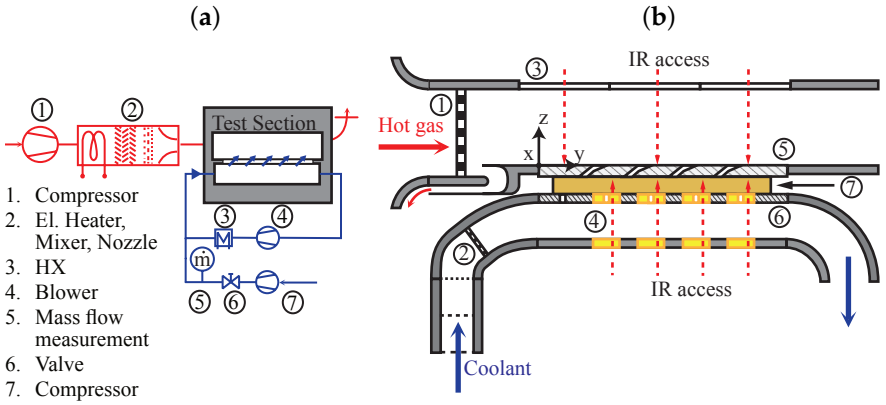

Figure 2. Test facility at ITS showing the hot gas path in red and the coolant path in blue. (**a**) Left Infrastructure, (**b**) right test section with ① Turbulence grid; ② Meshes, screens, and turbulence grid; ③ Sapphire windows; ④ Zinc-Selenide windows; ⑤ Specimen with effusion cooling pattern; ⑥ Specimen with impingement cooling pattern; ⑦ Polyetheretherketone (PEEK) frame around cavity.

The coolant air is provided in a semi-closed loop. Compressed air is supplied by a rotary screw compressor and discharged through a regulated valve into the closed loop coolant system. The amount of introduced air into the closed loop is tracked by a mass flow meter and equals the ejected coolant in the test section. Thus, the given blowing ratios are always averaged values over the whole effusion specimen.

To circulate the air in the closed loop section and to achieve engine similar coolant cross flow Reynolds numbers, a blower is integrated. To maintain constant air temperature, the heat input of the blower is removed with a heat exchanger.

2.1.1. Test Section

The central test section is a scaled, planar double-wall combustor design, shown in Figure 2, right side. Both the hot gas and the coolant channels are rectangular in cross section with parallel flow direction. They are connected via a cavity with an impingement plate on the coolant side and an effusion plate on the hot gas side.

The hot gas is introduced via the nozzle at the heater outlet. The exit width of the nozzle is $W_h = 500$ mm, and the height $H_h = 250$ mm. A turbulence grid generates an isotropic turbulence level of $Tu = 9.8\%$ (for design see [31]). Further downstream, a boundary layer bleed is installed to obtain a reproducible boundary layer thickness in the hot gas channel. After the boundary layer bleed, the channel height reduces to $H^* = 231$ mm. The test specimen is integrated in the bottom wall of the channel where the connecting surfaces up- and downstream and at the sides are isolated with low thermal conductivity material (PEEK). The effusion specimen's width and length are $W_{eff} = 280$ mm and $L_{eff} = 783$ mm.

The coolant channel has the same width and a height of $H_c = 150$ mm. The coolant flow channel inlet design (see ②) is adapted to increase coolant flow homogeneity (numerically designed and experimentally validated). The flow profile was further improved by introducing screens and meshes into the vertical portion of the coolant inlet. A tur-

bulence grid with $Tu = 5.0\%$ (same design principle as above) was added in the coolant flow channel.

The connecting cavity is introduced through plastic frame made of PEEK and sealed with polytetrafluoroethylene (PTFE) against both channels. The height of this frame defines the distance between the specimen as specified for the different geometrical setups. A shift in longitudinal direction between impingement and effusion specimen can be set (an optional lateral shift can be realized with the test setup; the data, however, are not presented in this article) by moving the impingement specimen. The geometrical configurations shown in this article are summarized in Table 1. This setup adds parallel cross flow conditions and thus simulates a combustor wall and engine realistic flow conditions, whereas most setups among different research papers (see Section 1.1) use plenum driven coolant ejection.

Table 1. Overview of geometrical test arrangements.

	Normal Al. (*MALO00*)	**Shifted Al. (*MALO05*)**
Cavity Height H	3D, 5D, 7D	3D, 5D, 7D
Longitudinal Shift $+S_y$	0.0	$0.5S$
Blowing ratios M	0.5, 1, 1.5, 2, 2.5, 3	0.5, 1, 1.5, 2, 2.5, 3

In the hot gas channel as well as in the coolant channel, various accesses exist for flow measurements to set the operating point and to record measurement data, which will be addressed in the section for measurement techniques. The final test conditions are shown in Table 2 for three of the six blowing ratios. By upscaling, a full similarity to engine conditions was achieved, most notably yielding high density ratios.

Table 2. Overview of flow conditions and operating conditions. Data are shown at three major blowing ratios, six analyzed in total. Deviation of values over all six different geometric test arrangements given for each blowing ratio.

Flow Conditions	$M = 1$	$M = 2$	$M = 3$
Hot Gas Inlet $T_{\mathrm{h,\,tot}}$	523 K $\pm$ 0.2%	523 K $\pm$ 0.1%	523 K $\pm$ 0.1%
Hot Gas $Re_{\mathrm{D,\,h}}$	1.916 $\pm$ 0.3%	1.916 $\pm$ 0.2%	1.915 $\pm$ 0.3%
Hot Gas Tu_{h}	9.8%	←	←
Coolant Inlet T_{c}	295 K $\pm$ 0.4%	295 K $\pm$ 0.3%	295 K $\pm$ 0.3%
Coolant Tu_{c}	5%	←	←
Coolant Crossflow $Re_{\mathrm{D,c}}$	4.231 $\pm$ 0.5%	4.231 $\pm$ 0.03%	4.237 $\pm$ 0.3%
Coolant Imp. $Re_{\mathrm{D,\,imp}}$	5.894 $\pm$ 0.9%	11.800 $\pm$ 0.5%	17.716 $\pm$ 0.5%
Operating Conditions			
Overall Pressure Drop $\Delta p/p$	0.74 $\pm$ 2.0%$_{\mathrm{rel}}$	2.20 $\pm$ 1.6%$_{\mathrm{rel}}$	4.23 $\pm$ 2.3%$_{\mathrm{rel}}$
Pressure Drop Ratio $\Delta p_{\mathrm{eff}}/\Delta p_{\mathrm{imp}}$	22.2 $\pm$ 1.3%$_{\mathrm{rel}}$	26.1 $\pm$ 1.0%$_{\mathrm{rel}}$	27.5 $\pm$ 1.3%$_{\mathrm{rel}}$
Density Ratio DR	1.78 $\pm$ 0.5%	1.81 $\pm$ 0.4%	1.85 $\pm$ 0.4%
Blowing Ratio M	1.0 $\pm$ 0.6%	2.0 $\pm$ 0.3%	3.0 $\pm$ 0.3%
Velocity Ratio VR	0.56 $\pm$ 0.6%	1.10 $\pm$ 0.4%	1.62 $\pm$ 0.3%
Momentum Flux Ratio I	0.56 $\pm$ 1.1%	2.21 $\pm$ 0.7%	4.87 $\pm$ 0.4%

2.1.2. Test Specimen

The scaling factor used for the engine geometry is $SF = 8$, resulting in a reference diameter of $D = 4$ mm. The specimen on the hot gas side with effusion holes has 159 laidback fan-shaped cooling holes distributed over 25 rows. In streamwise direction, the effusion hole pattern is shifted by $P/3$, i.e., the pattern repeats every 4th row as depicted in Figure 3. In streamwise direction, every row of cooling hole has a distance of $S = 6.67D$ to the next row. In a row, the pitch between each cooling hole is $P = 10D$. The effusion cooling holes are inclined by $\alpha = 30\,^{\circ}$ to the surface and have a cylindrical entry diameter of $E = \sqrt{2}D$.

The lateral opening angle and laidback opening angle are $\beta = 7\,^\circ$ (designed after the 7-7-7 configuration introduced by [32]).

The impingement specimen has vertical cylindrical cooling holes with a diameter of $D = 4\,\text{mm}$. Pitch and spacing of each cooling hole remain the same as for the effusion cooling holes, while their position is offset as described in Figure 3, right side. The chosen placement maximizes the wetted area on the backside of the effusion specimen before the coolant is ejected through the effusion cooling holes. For the misaligned setup *MALO05*, the impingement specimen is shifted by $S_y = 0.5P$ in longitudinal direction (y), placing the impingement exit opening on the rows of effusion entry holes. The origin for evaluation is placed at the start of the effusion specimen, in the lateral center of the channel.

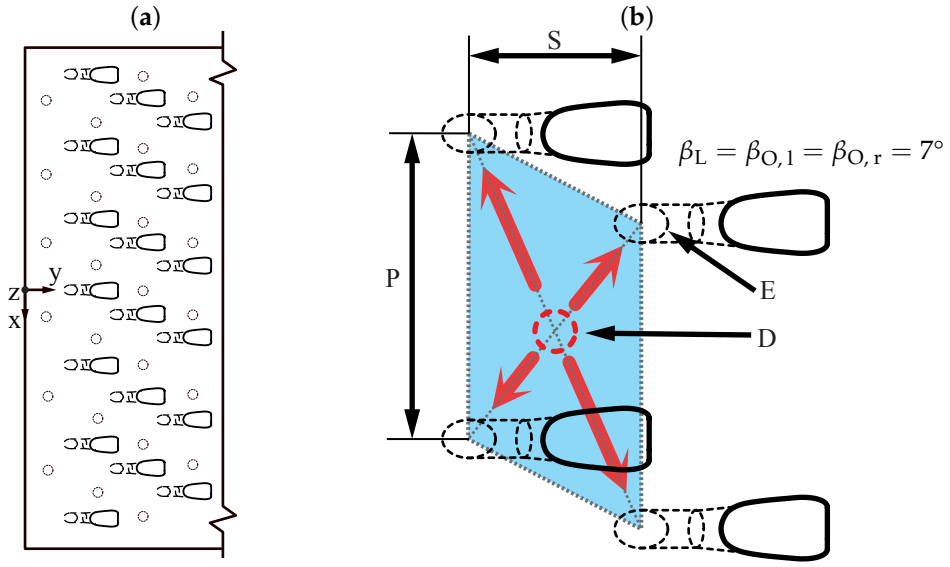

Figure 3. Test specimen geometry. Left, (**a**): Overall arrangement of the cooling holes for effusion and impingement specimen and coordinate frame. Right, (**b**): Arrangement of each impingement cooling hole to the effusion cooling holes. Red arrows show theoretical exit paths and distance to the next effusion cooling hole. The blue parallelogram shows the wetted area before the coolant is ejected. Both arrangements shown for $S_y = 0$.

The specimen with the effusion holes is made of TiAl6-V4 and has a thickness of $t_{\text{eff}} = 12\,\text{mm}$. The impingement plate is made of stainless steel AISI 420 with a thickness of $t_{\text{imp}} = 8\,\text{mm}$. The selection of material and thickness was derived from scaling the Biot number for a flat plate at jet engine conditions to experimental conditions.
The hydraulic porosity of the double-wall setup calculates to

$$A_e / A_{\text{tot}} = 1.02\,\% \tag{4}$$

with A_e being the total effective area of the impingement and effusion holes, and A_{tot} representing the total area of the specimen. For the calculation of the total effective area A_e, an incompressible relationship between mass flow rate and pressure difference is assumed. Thus, assuming constant density and a pressure drop distributed over both specimen $\Delta p = \Delta p_{\text{imp}} + \Delta p_{\text{eff}}$ (see also Table 2), this yields

$$A_e = \frac{1}{\sqrt{\left(\frac{1}{A_{\text{imp}}}\right)^2 + \left(\frac{1}{A_{\text{eff}}}\right)^2}}. \tag{5}$$

2.2. Measurement Methods and Derived Quantities

The main area of interest is the effusion-cooled specimen close to the hot gas side. For cooling and heat flux data, temperature field data are needed. The temperature data are acquired on both sides of the effusion specimen simultaneously using two infrared cameras. The access points are show in Figure 2, right side.

The hot gas side of the specimen is recorded using a FLIR SC6000 MWIR camera (Teledyne FLIR LLC, USA) with a short pass filter ($\lambda_{\mathrm{resp}} = 2$–$4.1\ \mu\mathrm{m}$). The short pass filter increases the data quality with hot sapphire windows [33]. Eight large sapphire windows give seamless access to the top surface. With the employed optical setup, a lateral width of 200 mm of the effusion specimen's surface is recorded at a resolution of $\approx 6\,\mathrm{px/mm}$—thus, lateral averages consider approximately five effusion holes per row.

The cavity side of the effusion specimen is accessed via four round windows ($D_{\mathrm{w}} = 100\,\mathrm{mm}$) in the impingement specimen. An InfraTec VarioCam hr head 720 researcher (Infratec GmbH, Germany) LWIR ($\lambda_{\mathrm{resp}} = 7$–$14\ \mu\mathrm{m}$) is used. The windows are made of ZnSe with an anti-reflective coating to allow LW transmissivity of $\tau = 90\%$. The windows are inset into and drilled with the impingement specimen pattern to avoid flow disturbance. Due to the anti-reflective coating and low angles of view, these holes only show a small temperature footprint in the final data. Temperature on the lower side of the effusion specimen is thus available at four streamwise locations, each in a circular shape. In each lateral direction, the hot gas recordings cover a wider area to mitigate boundary effects in the FE models presented below.

The data from the MWIR InSb detector are linearized ([34]). Otherwise, both cameras share similar calibration procedures. The data are corrected using a two-point non-uniformity correction (NUC) and then calibrated using a camera specific pre-calibration and a final in situ calibration [33]. With given temperatures, the residual non-uniformity is expected below $\Delta T_{\mathrm{rms}} \leq 0.5\,\mathrm{K}$ [35]. The measurement surfaces are coated using *Nextel Velvet Coating*, a high emissivity paint with $\varepsilon_{\mathrm{NVC}} \geq 0.94$ to reduce the effect of reflections (coating thickness $t_{\mathrm{NVC}} \approx 100\ \mu\mathrm{m}$). Due to the very low thermal conductivity of the coating ($\lambda_{\mathrm{NVC}} \approx 0.19\,\mathrm{W/(m\,K)}$, [36]), the thermal resistance is considered in the model and the evaluation of the FE analysis (see below). The final in situ calibration was performed using a single thermocouple for each image, choosing the position with the lowest expected heat flux to reduce thermocouple measurement uncertainty. Finally, the data are mapped to 3D space for further processing using a camera position estimation technique [37].

The heat flux data are derived using an FE model to compute heat fluxes from boundary temperatures. The model geometry is chosen so that the geometry represents a repeatable pattern, the top side is fully covered with measured temperatures, and the bottom side is mostly covered, leaving a small uncovered region outside of the final evaluation areas, the latter being the main constraint. The geometry is shown in Figure 4, left side view, for the hot gas side, and right side view for the cavity side. The colors show exemplary temperature data mapped from the infrared images for the access at position two. The perimeter walls are modeled as adiabatic due to the symmetry approach. The walls inside the cooling holes are modeled specifying a heat transfer coefficient and a constant sink temperature of 300 K. The heat transfer coefficient was derived from a Nusselt correlation for pipe flow evaluated at each operating point separately using the Reynolds numbers computed for the effusion holes. The resulting heat transfer coefficient ranges from $h \approx 30\,\mathrm{W/(m^2\,K)}$ for low blowing ratios up to $\approx 150\,\mathrm{W/(m^2\,K)}$ for high blowing ratios.

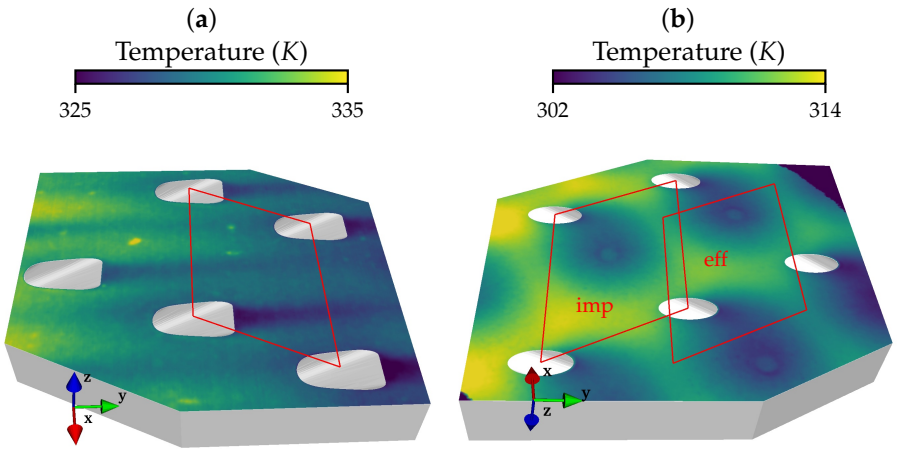

Figure 4. FE model for heat flux computation: left side (**a**) top view; right side (**b**) bottom view. Averaging areas for evaluation shown in red. Color shows mapped temperature from thermography of a case with $H = 5D$, *MALO00*.

The surfaces with measured temperatures have to consider the coating due to its thermal resistance behavior. This is included using a thin layer model with no lateral but high wall normal thermal resistance. The temperature measured with the thermography systems is subsequently applied to the outer side of the thin layer. Any calculation considering thermal conductivity uses surrogate values derived from the multiple layer model. The materials used in the model are considered with temperature-dependent thermal conductivity.

Using this approach, a discrete model can be built for each of the four access windows from below. The derived data in Section 3 are thus shown for each of the windows 1 to 4 and are averaged in three important areas of the model. These areas are shown in Figure 4 in red: one area on the top side which connects four effusion exit holes with a parallelogram shape, and two different areas on the bottom. The first area on the bottom side (subscript $_{\text{imp}}$) is defined as the wetted area (Figure 3), and the second area (subscript $_{\text{eff}}$) is defined as the $z-$shifted area from the top side.

Additionally, the hot gas channel was modeled and a radiation analysis was performed for each test case using the full coverage temperature data on the top side of the effusion side to derive the calorimetric irradiance heat flux. This radiation heat flux is then added as an additional boundary condition to the described FE models, thus yielding the true convective heat flux $\dot{q}_{\text{w}}$.

Thus, the heat transfer coefficient is defined as

$$h(x,y) = \frac{\dot{q}_{\text{w}}(x,y)}{T_{\text{ref}} - T_{\text{w}}(x,y)} \tag{6}$$

with T_{ref} being either the hot gas recovery temperature or the coolant recovery temperature. The reference temperatures are evaluated for each simulation separately from the data acquisition log files. This heat transfer coefficient is the used to derive Nusselt numbers and Biot numbers. The former are computed with the temperature-dependent heat conductivity of either coolant or hot gas, and the latter are computed using the effective thermal conductivity from the FE model, including effects of the coating and temperature dependence of material properties included in the FE model. This final post processing is performed using [38]—including automated data export and computation of derived quantities for each simulation.

Measurement uncertainty is derived by adding up several different sources. As described above, non-uniformity is expected below $\Delta T_{\text{rms}} \leq 0.5\,\text{K}$. The calibration thermocouple uncertainty is given with $\Delta T_{\text{tc}} \leq 1.5\,\text{K}$ for a type K class I thermocouple, which is,

however, shared between all measurements alike. Additional uncertainties are added when cross checking the final calibrated temperatures to other thermocouples not used for the calibration ($\Delta T_{\mathrm{tc,cal}} \leq 4\,\mathrm{K}$) and a positional uncertainty considering the low-conductivity paint ($\Delta T_{\mathrm{tc,p}} \leq 3\,\mathrm{K}$). Thus, the non-bias temperature error adds up to ΔT_{comb} = 3.5%, referenced on the temperature span between hot gas and coolant. For the FE simulations, this uncertainty has to be considered on both boundary sides alike, doubling its effective value. Assuming linear error propagation (which is not fully correct due to temperature-dependent material properties), this error propagates to heat fluxes and thus Nusselt and Biot numbers. Adding general modeling errors in the FE (e.g., uncertainty for in-hole boundary conditions, adiabatic modeling of perimeter), the final uncertainty is expected to be below $\Delta Nu \approx \Delta Bi \lessapprox 15\%$.

A validation of measurement data can only be performed checking plausibility by considering other data available. Comparing, e.g., impingement jet Nusselt numbers (quantity and shape, Figure 8) or total cooling effectiveness on the hot gas side, a good agreement with the available literature is found.

Additionally, several flow measurements are performed. In the hot gas channel, a pitot tube including a thermocouple and a static tap in the wall is used to measure the bulk velocity and temperature, and thus Reynolds number. The probe is placed in the center of the hot gas channel ($x = 0, y = -4D, z = 0.5H^*$). Additional probes at the channel side record static pressure in streamwise direction.

In the coolant channel, a pitot-static tube was used for bulk velocity measurements. Previously expressed concerns about unequal mass distribution in the coolant channel indicated that the usage of a pitot-static probe delivers more reliable results of bulk velocity measurements than a simpler pitot tube with a static port at the wall. The coolant temperature is monitored with a thermocouple probe. Additional pressure taps in the cavity (four along the streamwise direction) enable the measurement of pressure losses due to impingement cooling and effusion cooling separately. All parameters are constantly monitored and recorded, and the time used is resolved for the computation of relevant quantities.

3. Results and Discussion

The presented experimental setup allows the acquisition of both the hot gas and the cooling cavity side wall temperatures. Using FE models, heat fluxes and heat transfer coefficients can be derived in addition to total cooling effectiveness data. Compared to the previous work shown in Section 1.1, several unique features have been realized in this experimental setup. Coolant cross flow is introduced, mainly affecting the impingement jets. The measurements are performed at engine-similar density ratios and blowing ratios (thus momentum ratios). The temperature data are acquired simultaneously without affecting either hot gas or coolant flow. Two main geometrical variations have been identified and studied: the change in cavity height as a main design parameter and the relative alignment of effusion to the impingement specimen, which can occur due to thermal expansion in the real engine.

First, the overall cooling effectiveness from the hot gas side will be analyzed. Afterwards, a more detailed analysis of the cavity side heat transfer and the influence of different configurations will be described. Dimensionless quantities with subscript $_{\mathrm{D}}$ are always computed using the nominal impingement diameter. While all experiments were conducted at six different blowing ratios, the effect is mostly monotonous, and thus only the three major rates are displayed.

3.1. Cooling on the Hot Gas Side

The hot gas side total cooling effectiveness (Equation (1)) is shown in Figure 5 for the nominal cavity height of 5*D* and in Figure 6 for the smaller and larger cavity heights. Solid lines shows the aligned setup *MALO00*, and dashed lines show the misaligned setup *MALO05*.

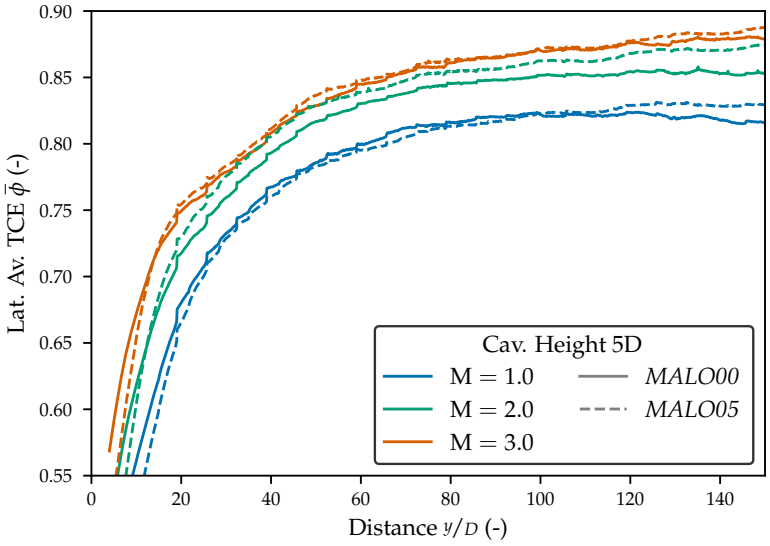

Figure 5. Laterally averaged total cooling effectiveness on hot gas side; nominal cavity height $5D$.

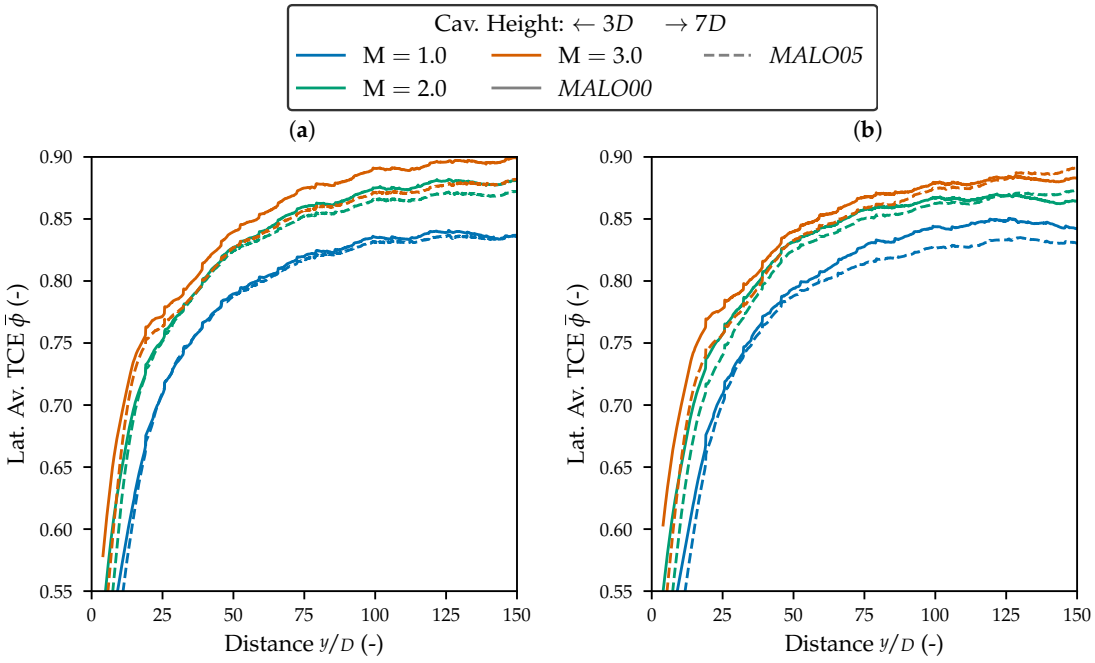

Figure 6. Laterally averaged total cooling effectiveness on hot gas side: (**a**) small cavity height $3D$, (**b**) large cavity height $7D$.

For all blowing ratios and all configurations, the general trend is comparable and in good agreement with previous research. The effusion cooling leads to a high total cooling effectiveness after short running lengths, and an asymptotic behavior is reached. The slope and the maximum value depend on blowing ratio, although with diminishing returns from $M \geq 2$ due to saturation effects in the coolant film layer. The achieved total cooling effectivenesses are high with $\bar{\phi} \geq 0.80$. At a nominal cavity height, a small improvement of total cooling effectiveness is visible for the misaligned configurations, which is most pronounced for a blowing ratio of $M = 2$. This presumably is explained by the changing flow pattern in the cavity which increases with increased impingement jet momentum. This increase in internal heat transfer is also visible in Figure A2. At the highest blowing ratio, this effect is negligible compared to the strong effusion cooling.

For small and large cavity heights, the geometrical alignment influence is more pronounced, with small cavities showing a reduction in effectiveness with increasing blowing

ratios. This presumably accounts for the complex, high momentum flow patterns in the confined cavity with a high influence on effusion flow. At large cavity heights, the reduction due to misalignment is more pronounced at lower blowing ratios, which results from reduced jet momentum and a reduction of local heat transfer at the jet impingement point on the back side of the effusion specimen. Thus, while the main contribution of cooling will be delivered by the protection from the effusion cooling, the impingement cooling can have a (comparably small) direct influence on total cooling effectiveness downstream; however, the effects of internal heat transfer and influence on effusion flow cannot be separated completely.

The heat transfer data on the hot gas side are shown in Figure 7 for the same blowing ratios and cavity heights using the same color coding. The Nusselt number is computed on the hot gas side and subsequently averaged in the parallelogram connecting four effusion holes, see Figure 4a—thus, a single scalar value is derived for each location. The standard deviation for each averaging process is given in Appendix A.

The Nusselt number decreases with running length mainly due to an increase in film protection. The gradient is the highest upstream where the film is still building. Nusselt numbers are low since they cover the full cooling solution (in contrary to data derived using, e.g., a superposition approach). Higher blowing ratios yield higher Nusselt numbers due to an increase in cavity side heat transfer—however, this is not the case for the smallest cavity height due to a difference in cavity flow patterns (see Figure 9).

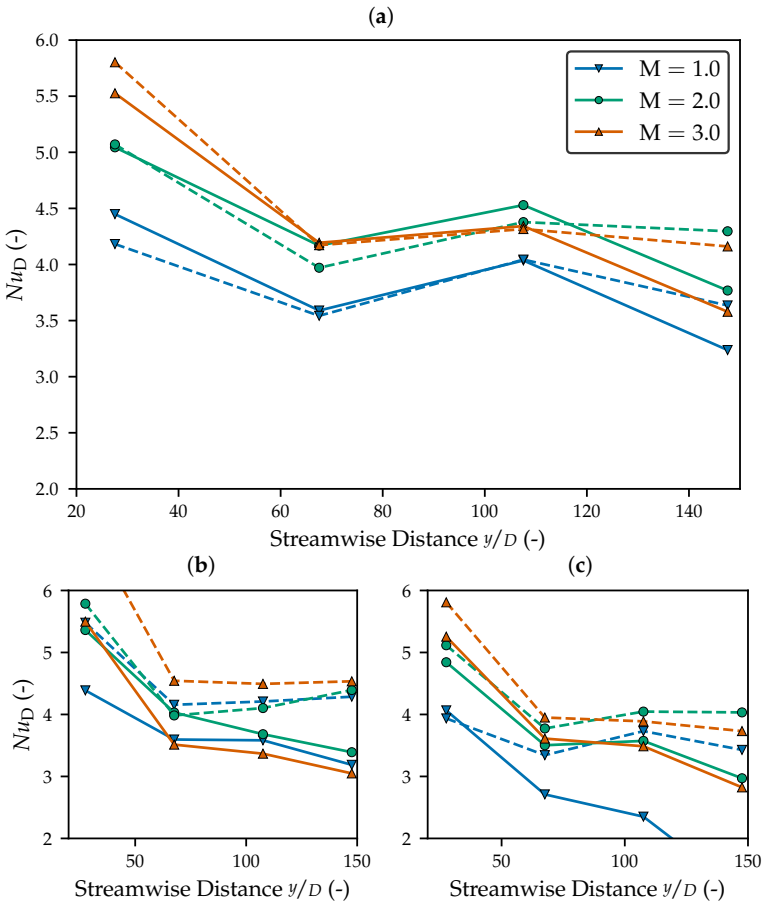

Figure 7. Nusselt numbers over streamwise length on the hot gas side of the effusion specimen averaged over area. (**a**) Nominal cavity height 5*D* at top, (**b**) small cavity height 3*D* bottom left, (**c**) large cavity height 7*D* bottom right. Solid lines show aligned setup *MALO00*; dashed lines show misaligned setup *MALO05*.

Another noticeable difference is visible comparing the two alignments *MALO00* and *MALO05* downstream on the test surface. In all cases, the misaligned setup shows higher Nusselt numbers in the last window's area, with the small cavity height showing the effect along all window accesses and also with the highest magnitude. The increase in Nusselt number at comparable surface total cooling effectivenesses points to an increased heat flux, driven by an increasing cavity side heat transfer. Additionally, the impingement location relative to the averaging area changes slightly, placing the geometrical impingement center at different positions relative to the averaged ares. This effect alone, however, has no major influence, as the other window locations and geometrical arrangements coincide—thus, the effect is determined by the complex flow patterns in case of the smallest cavity height.

3.2. Heat Transfer on Cavity Side

The heat transfer profile of a single jet is shown in Figure 8. The Nusselt number is plotted against the lateral distance at a line intersecting the impingement hole for each alignment (thus at different absolute $y-$positions) for all three cavity heights and two blowing ratios.

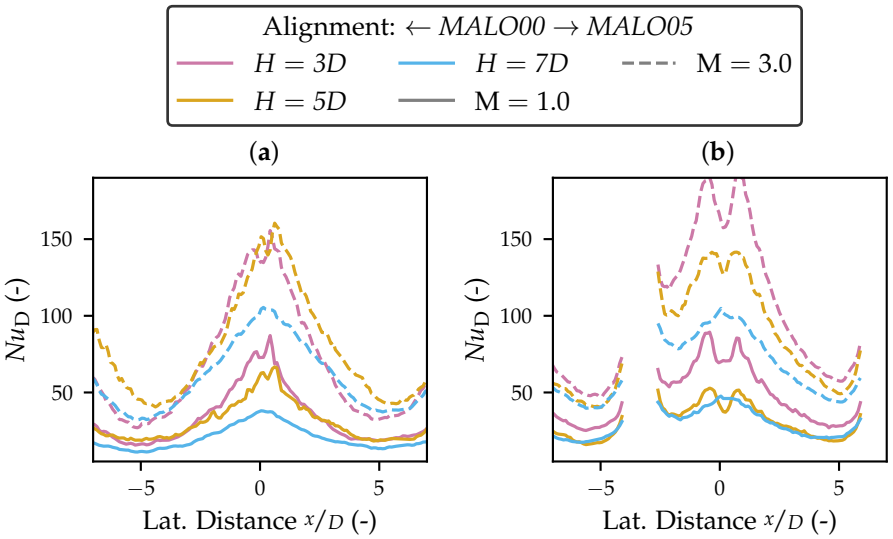

Figure 8. Nusselt number on the impingement side of the effusion specimen at the jet location. Different cavity heights and blowing ratios shown for (**a**) aligned case *MALO00* and (**b**) misaligned case *MALO05*.

The data are extracted at the location of the second window at $y/D \approx 65D$. The double-peak visible in some of the results is created by the distinct thermal footprint of the impingement hole edges in the circular windows (e.g., see Figures 2 and 4). In general, values are an order of magnitude higher than on the hot gas side, induced by the high impingement heat transfer coefficient and the comparably low temperature difference. Increasing the blowing ratio increase impingement heat transfer due to an increase in jet momentum, which is in good agreement with other impinging jet heat transfer research, e.g., [39,40]. For the nominally aligned case, the large cavity performs worse at low and high blowing ratios, while the other two cavity heights show little difference. With misalignment, two main differences are visible: the nominal cavity height of $5D$ performs worse at low blowing ratios, and the smallest cavity height of $3D$ performs substantially better at high blowing ratios. The latter is mainly influenced by high curvature in close-to-wall streamlines when the flow enters the effusion holes, yielding high local heat transfer coefficients. However, as described before and discussed in Figure 7, the laterally averaged total cooling effectiveness on the hot gas side still deteriorates presumably due to effusion hole flow reduction and uneven heat flux distributions on the cavity side.

This complex heat transfer distribution is shown for different configurations in Figure 9: at the high blowing ratio of $M = 3$, Nusselt number distributions are shown on the cavity side for the two alignments *MALO00* and *MALO05* (rows) at two different cavity heights $H = 3D$ and $H = 5D$ (columns).

The aligned configurations show the expected hexagonal flow pattern ([26]), leading to a maximized wetted area and optimized effusion hole inflow. The influence of cavity height is small with the small cavity height $H = 3D$ showing an increased jet heat transfer (see also Figure 7) in the impingement region. The large cavity height $H = 7D$ (not displayed) shows a decrease especially in impingement heat transfer. The misaligned cases, however, show a major influence of cavity height, as described earlier. Especially at low cavity heights, the jet impingement heat transfer peaks increase in intensity, with the demarcation lines becoming less pronounced as an indicator for a not well developed hexagonal pattern, complex mixing processes, and, in general, a more unordered flow pattern around the circular impingement area. At higher cavity heights of $H = 5D$, the effect is less pronounced and only small differences can be observed compared to the aligned case at the same nominal cavity height. While it is expected that the hexagonal flow patterns partly break down, a stable vortex system is most likely able to form in the increased cavity space, yielding an increased distribution and equalization of Nusselt numbers.

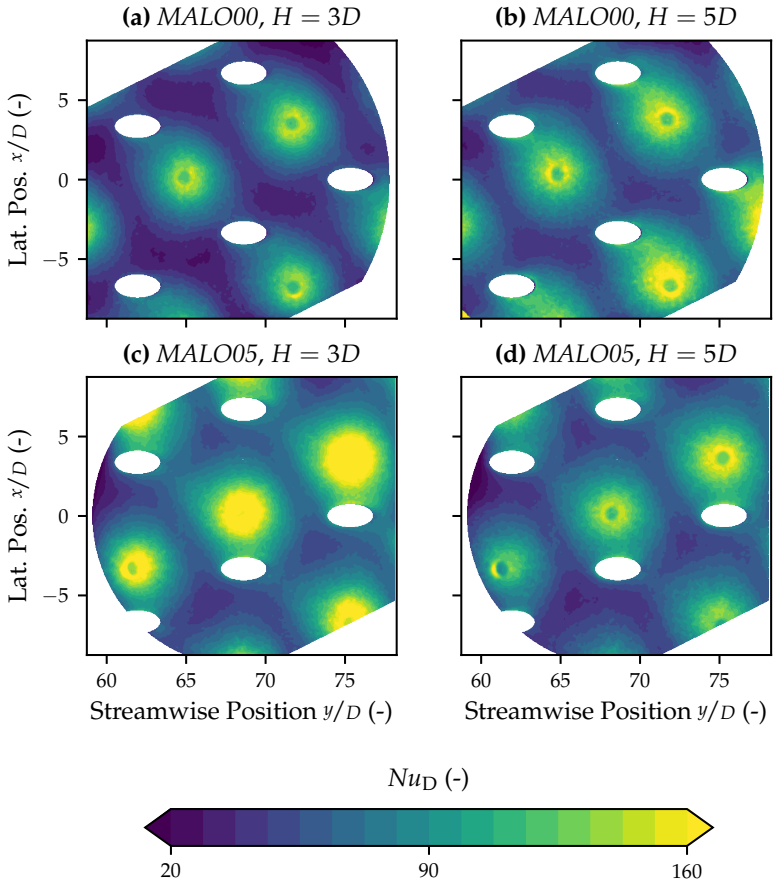

Figure 9. Nusselt number distributions on cavity side of effusion specimen for a high blowing ratio of $M = 3$. Rows show alignment; columns show different cavity heights.

The bottom side Nusselt numbers averaged at the four window locations are displayed in Figure A1 (impingement area in Figure 4) and Figure A2 (effusion area in Figure 4). Due to periodicity and comparable number of impinging jets in each area, the results are similar. Additional standard deviations are given in Appendix A in the Tables A1–A3. The absolute values are higher, and the deviations are more pronounced due to the complex heat transfer pattern induced by the impinging jet in the averaging area. For all cases displayed, a major

influence of blowing ratio is obvious. For the aligned cases, no significant difference in Nusselt numbers can be observed between the small cavity $H = 3D$ and the nominal cavity $H = 5D$. A decrease of heat transfer is visible for the large cavity height $H = 7D$, which confirms the results shown before. The Nusselt number increases downstream, especially at higher blowing ratios. With higher wall normal net heat fluxes, an improved jet heat transfer can be effectively used even with lower temperature differences. Additionally, the standard deviation increases due to the increased spatial inhomogeneity, with higher jet momentum leading to potentially increased thermal stresses, see Section 3.3.

An increase in Nusselt number is visible for the misaligned cases *MALO05* comparable to the hot gas side results (Figure 7). This effect increases with decreasing cavity height, as previously shown in the local Nusselt number distributions. This again is presumably due to more confined flow patterns with high streamline curvature. While high Nusselt numbers on the cavity side are favorable, the hot gas side data show that other effects have to be taken into account to determine the final total cooling effectiveness, and this effectiveness is still mostly influenced by the effusion cooling.

3.3. Thermal Gradients on the Cavity Side

Thermal gradients induced to the effusion specimen can be challenging for mechanical stability. In particular, the geometrically complex effusion holes with sharp edges at the angled inlets can deteriorate quickly under low-cycle fatigue thermal loads. Due to correct scaling, including Biot similarity, experimental data, in this case the Biot number itself, can be used as an indicator for thermal gradients and thus thermal stresses in the engine environment, especially those induced by the jet impingement heat transfer at the cavity side of the effusion specimen. The Biot number distributions on the cavity side are shown for the two cavity heights $H = 3D$ and $H = 5D$ and the two alignments *MALO00* and *MALO05* at the high blowing ratio $M = 3$ in Figure A3. Columns show the four window positions for each configuration. The color scale is kept the same for each plot for increased compatibility.

For all configurations shown, an increase in Biot number is visible with main flow streamwise length, mainly due to increased heat transfer coefficient as shown in the previous section. Again, this increase is more pronounced with the misaligned configurations—the aligned configurations' average Biot number does not increase for window three and four and, in case of the nominal cavity height $H = 5D$, even decreases slightly. Each configuration shows similar Biot number patterns at each individual window location; however, the mean level changes. This is in good agreement with the previously described similarity of cavity flow at each position.

Both the small and the nominal cavity height at the aligned setup show low Biot numbers at each location with a comparably homogeneous flow field (excluding the impingement location). A well-formed flow pattern and effective effusion inflow are assumed. The cases with misalignment *MALO05* show substantially higher Biot numbers and also higher Biot number gradients. This distribution can lead to increased thermal stresses, which are exacerbated by the effect of high Biot numbers close to the effusion inflow holes where low material thicknesses and sharp corners are present. This inhomogeneity close to the effusion inflow holes is again presumably related to a disturbance of optimal hexagonal flow in the cavity and thus even more pronounced with small cavity heights.

The Biot number distributions show that the alignment of the two specimens can especially have a major influence on thermal gradients, with little influence visible in total cooling effectiveness on the hot gas side. Thus, regarding thermal stresses, an optimal alignment as proposed with the *MALO00* setup is recommended.

4. Conclusions

A double-wall design for an intensively cooled combustor has been analyzed extensively in a test rig under engine-similar, scaled conditions. The double-wall consists of an outer impingement specimen and an inner effusion specimen with laidback fan-shaped

cooling holes. Surface temperature data have been acquired using thermography on both sides of the effusion specimen simultaneously. Heat transfer data subsequently were derived using a segment FE model. The experiments were performed with coolant cross flow at engine-similar Reynolds numbers.

Some drawbacks with this approach have to be kept in mind: with the current setup, no true superposition approach or derivation of adiabatic wall temperatures on either side is possible. Thus, a separation of the different contributions to the total cooling effectiveness cannot be derived directly and must be identified by the global data. The application of superposition may be added in future work by using different wall materials; however, Biot similarity will not be achievable. Additionally, the effect of different in-hole boundary conditions in the FE model can and needs to be analyzed, considering better approximations for the heat transfer coefficient as shown in most recent references.

Analyzing the extensive experimental data presented leads to the following conclusion.

- Using a double-wall configuration with impingement effusion cooling can achieve very high total cooling effectivenesses on the inner hot gas side, especially considering full conjugate heat transfer. The main cooling contribution, in particular downstream where the effusion coolant film is built up, comes from the very same. After short running lengths downstream of the initial effusion row, total cooling effectivenesses up to $\bar{\phi} \geq 0.8$ are achieved (lateral average).
- The influence of impingement cooling was found to be marginal in the single digit percentage considering the hot gas side total cooling effectiveness. This influence is more pronounced upstream with the effusion cooling, which is, however, derived from other studies and only marginally visible in the total cooling effectiveness with superposition data missing.
- The effect of geometry variation is especially pronounced in the cavity flow and thus cavity side heat transfer. The analyzed misaligned configurations show a strong influence of cavity height (small and nominal height), while the aligned configurations are less influenced. The largest cavity height of $H = 7D$ shows a decreased heat transfer performance at any alignment, especially at low blowing ratios.
- Biot numbers and thus thermal gradients show comparable behavior. The misaligned cases with small and nominal cavity height especially show high Biot numbers and Biot number gradients at the effusion inflow locations, which can lead to material deterioration during service.

Thus, due to the small influence on total cooling effectiveness, cavity height and alignment can be chosen to reduce thermal stresses and to optimize aerodynamics for a given use case. The nominal cavity height of $H = 5D$ with aligned setup *MALO00* proved to be the best overall solution for this setup.

Comparing the results to recent work available shows a good agreement. Hot gas total cooling effectiveness is, in general, found to be very high with the employed double-wall combustor liner concept ([22,23]), with effective Nusselt numbers being comparably low ([15,17]). Data on the cooling side are less comparable due to the novel introduction of coolant cross flow at engine-similar Reynolds numbers. Additionally, most available data on the cavity side are based on CFD. Nusselt numbers at the jet impingement location are in good agreement with data acquired at similar jet conditions ([6,11]). Comparing the results with more general impinging jet research, Nusselt numbers are still well comparable [40].

The new design possibilities using a double-wall concept and thus a staged pressure drop allow for the optimization of effusion cooling. By decreasing the effusion cooling pressure, head porosity can be increased. An increased area will subsequently increase total convective heat transfer inside the effusion holes and effectively reduce the momentum ratio, both pertinent to high effusion cooling efficiencies and a stable combustion. This path of optimization will be analyzed in future studies. Future work will also include the analysis of a lateral misalignment of the two specimens, of which the test setup is already prepared. Combined with the longitudinal misalignment present in this study, an almost arbitrary relative positioning of the two-wall specimen is possible.

Author Contributions: Each author has contributed equally to this version of the manuscript. The work has been prepared in close collaboration between the authors, and there is no strict separation between text passages. All authors have read and agreed to the published version of the manuscript.

Funding: This project was supported by the Federal Ministry for Economic Affairs and Energy, Germany, in the framework of the LuFo-the Federal Aviation Research Programme. We acknowledge support by the KIT-Publication Fund of the Karlsruhe Institute of Technology.

Data Availability Statement: The data presented in this study are available on request from the corresponding author. The data are not publicly available due to the large amounts of data. In addition to the thermal results presented in this article, aerodynamic data (HSPIV) are also available for the same test setup.

Conflicts of Interest: The authors declare no conflict of interest.

Abbreviations

The following abbreviations and symbols are used in this manuscript:

Symbols

Δ	Difference
α	Hole inclination
β	Laidback and fanshape angle
ε	Emissivity
λ	Wavelength
ϕ	Total cooling effectiveness
τ	Transmissivity
A	Area
D	Reference diameter, diameter
DR	Density ratio
E	Effusion hole diameter
H	Height
h	Heat transfer coefficient
I	Momentum ratio
k	Heat conductivity
L	Length
M	Blowing ratio M
P	Pitch
p	Pressure
q	Heat flux
S	Shift
SF	Scaling factor
T	Temperature
Tu	Turbulence level
t	Thickness
VR	Velocity ratio
W	Width

Abbreviations

Bi	Biot number
FE	Finite elements
ITS	Institute of Thermal Turbomachinery
LW	Long-wave (infrared)
MALO	Longitudinal misalignment
MW	Mid-wave (infrared)
Nu	Nusselt number
PEEK	Polyetheretherketone

PTFE	Teflon ™
Re	Reynolds number
RQL	Rich-quench-lean
Scripts	
∞	Free stream
$''$, f	Film cooling
aw	Adiabatic wall
c	Cold
cal	Calibrated
comb	Combined
e	Effective
eff	Effusion
h	Hot
imp	Impingement
int	Internal
L	Laidback (angle)
tc	Thermocouple
NVC	Nextel velvet coating
O	Opening (angle)
p	Paint
tot	Total
w	Wall, window

Appendix A. Additional Data

Table A1. Standard deviations of hot gas side Nusselt number for each of the averaged data points shown in Figure 7.

	M = 1					**M = 2**					**M = 3**				
	Wind. #					***Wind. #***					***Wind. #***				
MALO00	**1**	**2**	**3**	**4**	**Avg.**	**1**	**2**	**3**	**4**	**Avg.**	**1**	**2**	**3**	**4**	**Avg.**
3*D*	1.07	0.54	0.48	0.42	0.63	1.20	0.66	0.60	0.47	0.73	1.26	0.58	0.47	0.40	0.68
5*D*	1.25	0.53	0.52	0.38	0.67	1.30	0.58	0.59	0.56	0.76	1.34	0.62	0.56	0.44	0.74
7*D*	1.20	0.50	0.44	0.30	0.61	1.23	0.51	0.51	0.39	0.66	1.29	0.58	0.50	0.41	0.70
MALO05															
3*D*	1.01	0.49	0.50	0.51	0.63	1.09	0.52	0.57	0.56	0.73	1.20	0.65	0.57	0.56	0.68
5*D*	1.23	0.50	0.52	0.47	0.67	1.33	0.67	0.59	0.53	0.76	1.28	0.62	0.60	0.53	0.74
7*D*	1.13	0.52	0.46	0.40	0.61	1.20	0.56	0.52	0.51	0.66	1.25	0.61	0.52	0.50	0.70

Table A2. Standard deviations of cavity side Nusselt number for each of the averaged data points (*imp* area) shown in Figure A1.

	M = 1					**M = 2**					**M = 3**				
	Wind. #					***Wind. #***					***Wind. #***				
MALO00	**1**	**2**	**3**	**4**	**Avg.**	**1**	**2**	**3**	**4**	**Avg.**	**1**	**2**	**3**	**4**	**Avg.**
3*D*	9.61	12.48	14.29	13.53	12.48	16.78	28.07	32.57	42.24	29.92	21.63	27.43	47.70	72.55	42.33
5*D*	8.03	10.14	11.90	9.70	9.94	11.55	18.09	26.15	20.22	19.00	16.02	27.30	51.01	46.37	35.18
7*D*	6.65	7.40	7.68	5.67	6.85	10.92	13.72	16.79	13.91	13.84	14.88	18.76	22.51	19.16	18.83
MALO05															
3*D*	11.59	13.84	16.96	16.93	12.48	17.54	20.24	29.51	52.39	29.92	31.27	32.52	66.10	179.63	42.33
5*D*	7.97	8.96	12.51	10.14	9.94	13.55	17.49	28.30	45.91	19.00	18.14	24.65	39.96	100.87	35.18
7*D*	5.91	7.41	9.48	7.62	6.85	9.55	12.20	18.01	24.85	13.84	12.65	16.19	23.40	44.37	18.83

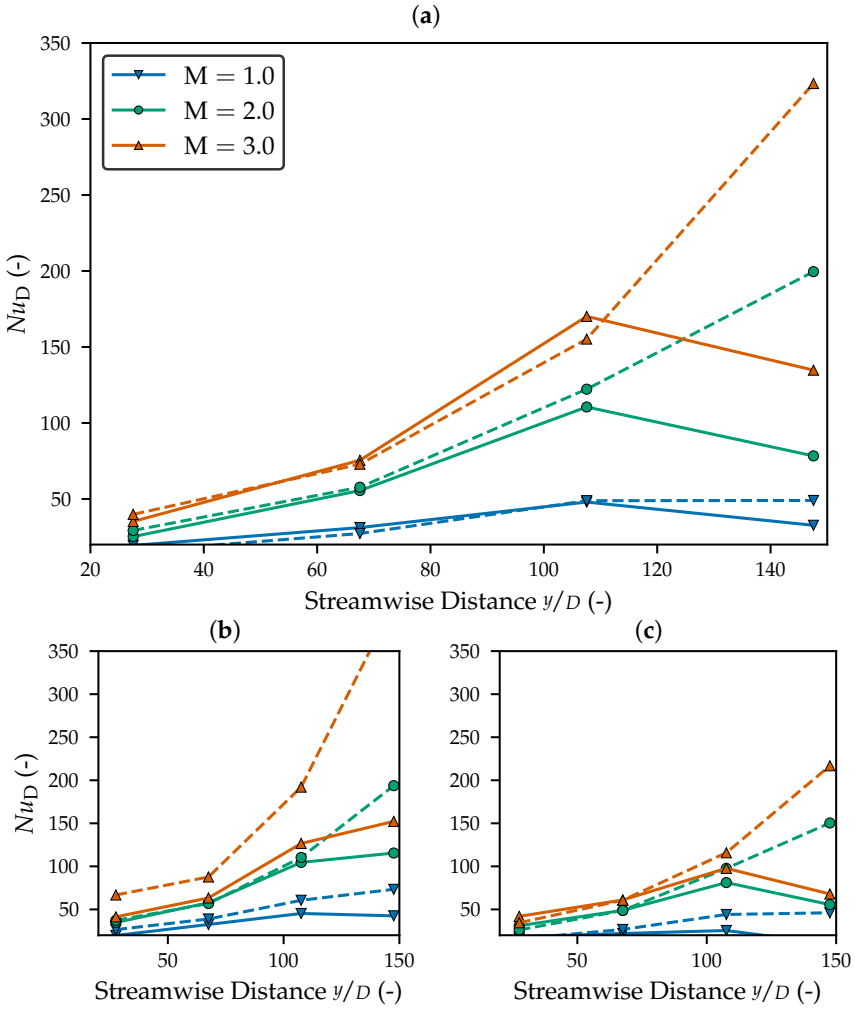

Figure A1. Nusselt numbers over streamwise length on the cavity side of the effusion specimen averaged in the *imp* area. (**a**) Nominal cavity height 5*D* at top, (**b**) small cavity height 3*D* bottom left, (**c**) large cavity height 7*D* bottom right. Solid lines show aligned setup *MALO00*; dashed lines show misaligned setup *MALO05*.

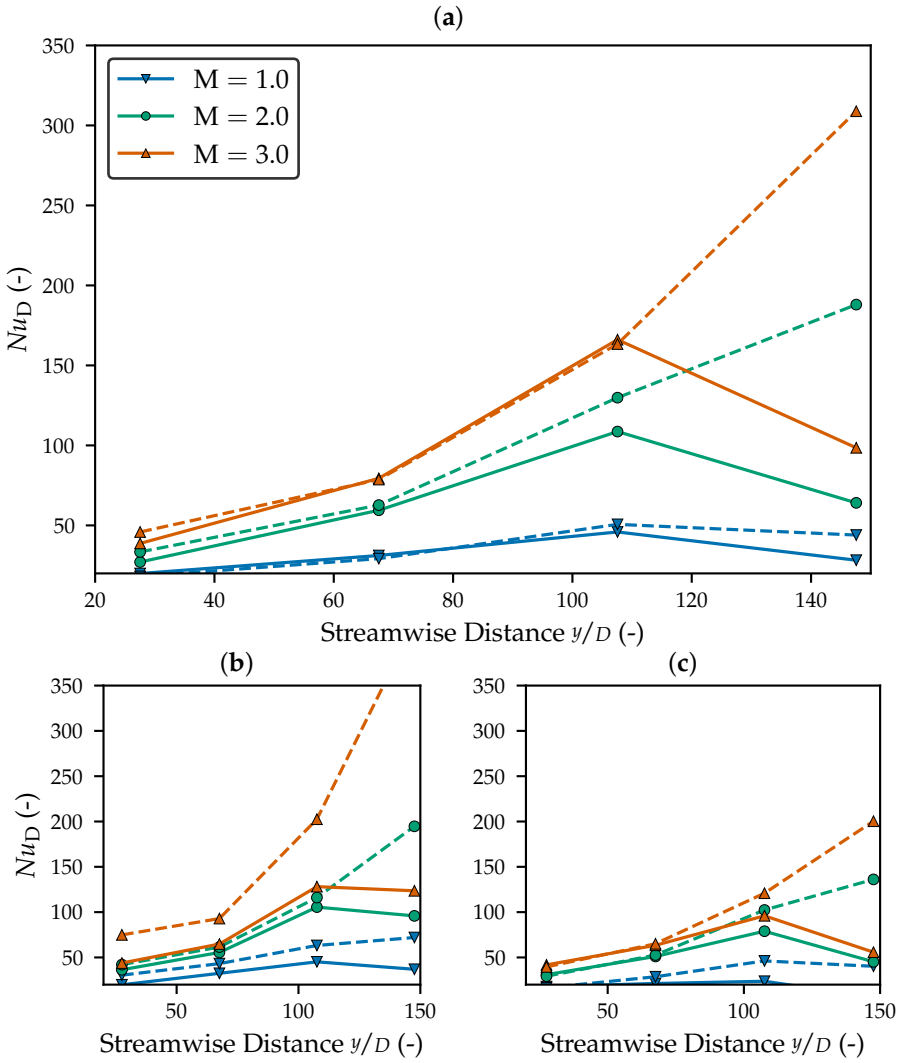

Figure A2. Nusselt numbers over streamwise length on the cavity side of the effusion specimen averaged in the *eff* area. (**a**) Nominal cavity height 5*D* at top, (**b**) small cavity height 3*D* bottom left, (**c**) large cavity height 7*D* bottom right. Solid lines show aligned setup *MALO00*; dashed lines show misaligned setup *MALO05*.

Table A3. Standard deviations of cavity side Nusselt number for each of the averaged data points (*eff* area) shown in Figure A2.

	M = 1					**M = 2**					**M = 3**				
	Wind. #					***Wind. #***					***Wind. #***				
MALO00	**1**	**2**	**3**	**4**	**Avg.**	**1**	**2**	**3**	**4**	**Avg.**	**1**	**2**	**3**	**4**	**Avg.**
3*D*	10.00	12.29	12.87	11.01	11.54	17.67	19.43	29.45	29.84	24.10	22.62	27.58	45.32	50.26	36.44
5*D*	8.22	9.55	10.55	7.52	8.96	11.91	17.99	23.43	15.24	17.14	16.97	28.59	46.51	31.25	30.83
7*D*	6.77	7.21	7.43	5.06	6.62	11.15	13.50	15.47	10.68	12.70	15.02	18.31	21.50	14.54	17.35
MALO05															
3*D*	12.35	14.74	17.73	19.29	11.54	18.63	22.11	33.79	60.82	24.10	34.02	36.55	74.93	205.41	36.44
5*D*	7.73	9.40	12.63	11.23	8.96	13.76	19.29	32.55	52.36	17.14	18.72	27.38	45.06	114.48	30.83
7*D*	5.87	7.64	9.65	9.00	6.62	9.64	12.81	19.29	28.33	12.70	13.06	17.14	25.11	48.72	17.35

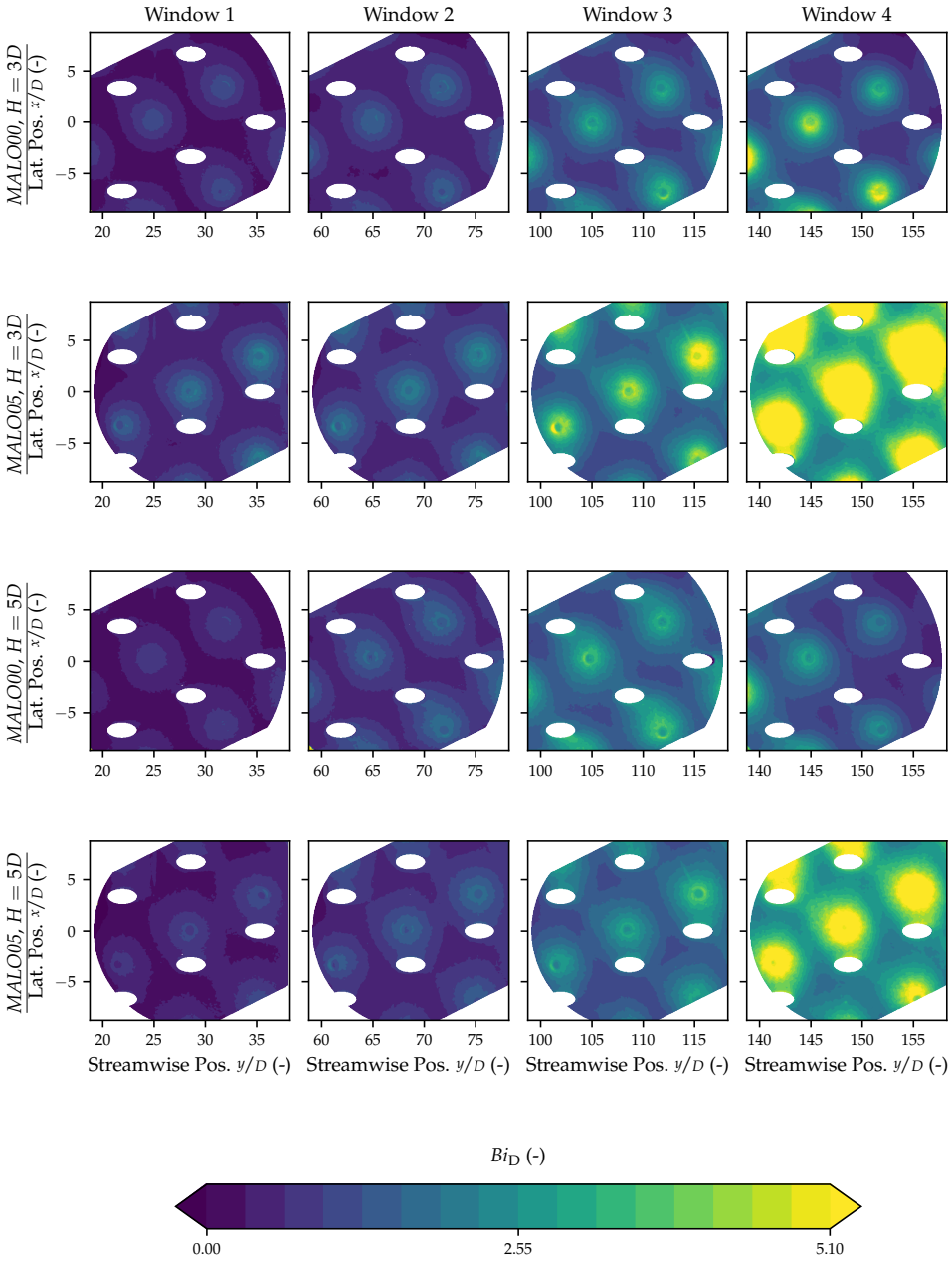

Figure A3. Biot number distributions on cavity side of effusion specimen. Rows show selected configurations; columns show window position.

References

1. Lefebvre, A.H.; Ballal, D.R. *Gas Turbine Combustion: Alternative Fuels and Emissions*, 3rd ed.; Taylor & Francis: Boca Raton, FL, USA, 2010.
2. Lazik, W.; Doerr, T.; Bake, S.; vd Bank, R.; Rackwitz, L. Development of Lean-Burn Low-NOx Combustion Technology at Rolls-Royce Deutschland. In Proceedings of the ASME Turbo Expo, Berlin, Germany, 9–13 June 2008; p. GT2008-5115. [CrossRef]
3. Sweeney, P.C.; Rhodes, J.F. An Infrared Technique for Evaluating Turbine Airfoil Cooling Designs. *J. Turbomach.* **1999**, *122*, 170–177. [CrossRef]
4. Andrews, G.E.; Asere, A.A.; Hussain, C.I.; Mkpadi, M.C.; Nazari, A. Impingement/Effusion Cooling: Overall Wall Heat Transfer. In Proceedings of the ASME 1988 International Gas Turbine and Aeroengine Congress, Amsterdam, The Netherlands, 6 June 1988; p. V004T09A036. [CrossRef]

5. Al Dabagh, A.M..; Andrews, G.E.; Abdul Husain, R.A.A..; Husain, C.I.; Nazari, A.; Wu, J. Impingement/Effusion Cooling: The Influence of the Number of Impingement Holes and Pressure Loss on the Heat Transfer Coefficient. *J. Turbomach.* **1990**, *112*, 467. [CrossRef]
6. El-Jummah, A.; Nazari, A.; Andrews, G.E.; Staggs, J.E. Impingement/Effusion Cooling Wall Heat Transfer: Reduced Number of Impingement Jet Holes Relative to the Effusion Holes. In Proceedings of the ASME Turbo Expo, Charlotte, NC, USA, 26–30 June 2017; p. GT2017-63494. [CrossRef]
7. Oguntade, H.I.; Andrews, G.E.; Burns, A.D.; Ingham, D.B.; Pourkashanian, M. Impingement/Effusion Cooling with Low Coolant Mass Flow. In Proceedings of the ASME Turbo Expo Charlotte, NC, USA, 26–30 June 2017; p. GT2017-63484. [CrossRef]
8. Martiny, M.; Schulz, A.; Wittig, S. Effusion Cooled Combustor Liners of Gas Turbines—An Assessment of the Contributions of Convective, Impingement, and Film Cooling. In Proceedings of the Symposium on Energy Engineering in the 21st Century (SEE2000), Hong Kong, China, 9–13 January 2000; pp. 221–228.
9. Andreini, A.; Caciolli, G.; Facchini, B.; Tarchi, L.; Coutandin, D.; Taddei, S.; Peschiulli, A. Combustor Liner Cooled By a Combined Slot/Effusion System. In Proceedings of the ASME Turbo Expo, Copenhagen, Denmark, 11–15 June 2012; p. GT2012-68263. [CrossRef]
10. Cocchi, L.; Picchi, A.; Mazzei, L.; Andreini, A.; Belloci, L. Effect of Holes Arrangement on Heat Transfer in Impingement/Effusion Cooling Double Wall Schemes. In Proceedings of the 1st GPPS, Zurich, Switzerland, 16–18 January 2017; p. GPPF-2017-77.
11. Chen, G.; Liu, Y.; Rao, Y.; He, J.; Qu, Y. Numerical Investigation on Conjugate Heat Transfer of Impingement/Effusion Double-Wall Cooling with Different Crossflow Schemes. *Appl. Therm. Eng.* **2019**, *155*, 515–524. [CrossRef]
12. Rogers, N.; Ren, Z.; Buzzard, W.; Sweeney, B.; Tinker, N.; Ligrani, P.M. Effects of Double Wall Cooling Configuration and Conditions on Performance of Full Coverage Effusion Cooling. In Proceedings of the ASME Turbo Expo, Seoul, Korea, 13–17 June 2016; p. GT2016-56515. [CrossRef]
13. Ligrani, P.; Ren, Z.; Liberatore, F.; Patel, R.; Srinivasan, R.; Ho, Y.H. Double Wall Cooling of a Full-Coverage Effusion Plate, Including Internal Impingement Array Cooling. *J. Eng. Gas Turbines Power* **2017**, *140*, 051901. [CrossRef]
14. Click, A.; Ritchie, D.; Ligrani, P.M.; Liberatore, F.; Patel, R.; Ho, Y.H. Double Wall Cooling of an Effusion Plate with Cross Flow and Impingement Jet Combination Internal Cooling: Comparisons of Main Flow Contraction Ratio Effects. In Proceedings of the AIAA Propulsion and Energy 2019 Forum. American Institute of Aeronautics and Astronautics, Indianapolis, IN, USA, 19–22 August 2019. [CrossRef]
15. Click, A.; Ligrani, P.; Ritchie, D.; Liberatore, F.; Patel, R.; Ho, Y.H. Effects of Coolant Supply Arrangement on Double Wall Cooling: Hot-side Effusion Performance and Cold-Side Nusselt Numbers at Different Initial Blowing Ratios. *Int. J. Heat Mass Transf.* **2020**, *156*, 119808. [CrossRef]
16. Vanga, S.R.; Ritchie, D.; Click, A.; Ren, Z.; Ligrani, P.; Liberatore, F.; Patel, R.; Srinivasan, R.; Ho, Y.H. Double Wall Cooling of a Full-Coverage Effusion Plate With Main Flow Pressure Gradient, Including Internal Impingement Array Cooling. *J. Turbomach.* **2019**, *141*, 041002. [CrossRef]
17. Vanga, S.R.; Ligrani, P.M.; Knox, J.; Liberatore, F.; Patel, R.; Ho, Y.H. Louver and effusion cooling heat transfer for a double wall effusion plate with impingement jet array coolant supply. *Int. J. Heat Mass Transf.* **2021**, *168*, 120861. [CrossRef]
18. Ngetich, G.C.; Murray, A.V.; Ireland, P.T.; Romero, E. A Three-Dimensional Conjugate Approach for Analysing a Double-Walled Effusion-Cooled Turbine Blade. *J. Turbomach.* **2019**, *141*, 011002. [CrossRef]
19. Ngetich, G.C.; Ireland, P.T.; Romero, E. Study of Film Cooling Effectiveness on a Double-Walled Effusion-Cooled Turbine Blade in a High-Speed Flow Using Pressure Sensitive Paint. In Proceedings of the ASME Turbo Expo, Phoenix, AZ, USA, 17–21 June 2019; p. GT2019-90545. [CrossRef]
20. Murray, A.V.; Ireland, P.T.; Rawlinson, A.J. An Integrated Conjugate Computational Approach for Evaluating the Aerothermal and Thermomechanical Performance of Double-Wall Effusion Cooled Systems. In Proceedings of the ASME Turbo Expo, Charlotte, NC, USA, 26–30 June 2017; p. GT2017-64711. [CrossRef]
21. Murray, A.V.; Ireland, P.T.; Romero, E. Development of a Steady-State Experimental Facility for the Analysis of Double-Wall Effusion Cooling Geometries. *J. Turbomach.* **2019**, *141*, 041008. [CrossRef]
22. Murray, A.V.; Ireland, P.T.; Romero, E. Experimental and Computational Methods for the Evaluation of Double-Wall, Effusion Cooling Systems. *J. Turbomach.* **2020**, *142*, 111003. [CrossRef]
23. Shrager, A.C.; Thole, K.A.; Mongillo, D. Effects of Effusion Cooling Pattern Near the Dilution Hole for a Double-Walled Combustor Liner-Part 1: Overall Effectiveness Measurements. *J. Eng. Gas Turbines Power* **2019**, *141*, 10. [CrossRef]
24. Shrager, A.C.; Thole, K.A.; Mongillo, D. Effects of Effusion Cooling Pattern Near the Dilution Hole for a Double-Walled Combustor Liner-Part II: Flowfield Measurements. *J. Eng. Gas Turbines Power* **2019**, *141*, 10. [CrossRef]
25. Huelsmann, N.C.; Thole, K.A. Effects of Jet Impingement on Convective Heat Transfer in Effusion Holes. *J. Turbomach.* **2021**, *143*, 10. [CrossRef]
26. Jackowski, T.; Elfner, M.; Bauer, H.J. Numerical Investigation of Conjugate Heat Transfer in an Effusion and Impingement Cooled Combustor Wall. In Proceedings of the ASME Turbo Expo, Online, 21–25 September 2020; p. GT2020-15505.
27. Goldstein, R.J. Film Cooling. In *Advances in Heat Transfer*; Elsevier: Amsterdam, The Netherlands, 1971; pp. 321–379. [CrossRef]
28. Choe, H.; Kays, W.M.; Moffat, R.J. The Superposition Approach to Film-Cooling. In Proceedings of the American Society of Mechanical Engineers, New York, NY, USA, 17–22 November 1974; Volume 74-WA.

29. Albert, J.E.; Bogard, D.G.; Cunha, F. Adiabatic and Overall Effectiveness for a Film Cooled Blade. In Proceedings of the ASME Turbo Expo 2004, Vienna, Austria, 14–17 June 2004. [CrossRef]
30. Nathan, M.L.; Dyson, T.E.; Bogard, D.G.; Bradshaw, S.D. Adiabatic and Overall Effectiveness for the Showerhead Film Cooling of a Turbine Vane. *J. Turbomach.* **2013**, *136*, 031005. [CrossRef]
31. Roach, P. The Generation of Nearly Isotropic Turbulence by Means of Grids. *Int. J. Heat Fluid Flow* **1987**, *8*, 82–92. [CrossRef]
32. Schroeder, R.P.; Thole, K.A. Adiabatic Effectiveness Measurements for a Baseline Shaped Film Cooling Hole. In *Volume 5B: Heat Transfer*; American Society of Mechanical Engineers: New York, NY, USA, 2014. [CrossRef]
33. Ochs, M.; Horbach, T.; Schulz, A.; Koch, R.; Bauer, H.J. A Novel Calibration Method for an Infrared Thermography System Applied to Heat Transfer Experiments. *Meas. Sci. Technol.* **2009**, *20*, 9. [CrossRef]
34. Ochs, M.; Schulz, A.; Bauer, H.J. High Dynamic Range Infrared Thermography by Pixelwise Radiometric Self Calibration. *Infrared Phys. Technol.* **2010**, *53*, 112–119. [CrossRef]
35. Elfner, M.; Schulz, A.; Bauer, H.J. Surface Temperature Measurement on Complex Topology by Infrared Thermography. In *The Art of Measuring in the Thermal Sciences*, 1st ed.; Meyer, J.P., De Paepe, M., Eds.; Taylor and Francis Group: Boca Raton, FL, USA, 2020; Chapter 10, p. 482.
36. Lohrengel, J.; Todtenhaupt, R. Wärmeleitfähigkeit, Gesamtemissionsgrade und spektrale Emissionsgrade der Beschichtung Nextel Velvet Coating 811-21. *PTB-Mitteilungen* **1996**, *106*, 259–265.
37. Elfner, M.; Schulz, A.; Bauer, H.J.; Lehmann, K. Comparative Experimental Investigation of Leading Edge Cooling Concepts of Turbine Rotor Blades. In Proceedings of the ASME Turbo Expo, Oslo, Norway, 11–15 June 2018; p. GT2018-75360. [CrossRef]
38. Hennig, J.; Elfner, M.; Feder, J. *MPh*; OpenSource Software; Zendo: Geneva, Switzerland, 2021. [CrossRef]
39. O'Donovan, T.S.; Murray, D.B. Jet Impingement Heat Transfer-Part I: Mean and Root-Mean-Square Heat Transfer and Velocity Distributions. *Int. J. Heat Mass Transf.* **2007**, *50*, 3291–3301. [CrossRef]
40. Sagot, B.; Antonini, G.; Christgen, A.; Buron, F. Jet Impingement Heat Transfer on a Flat Plate at a Constant Wall Temperature. *Int. J. Therm. Sci.* **2008**, *47*, 1610–1619. [CrossRef]